Published in final edited form as:
NMR Biomed. 2013 April ; 26(4): 424–435. doi:10.1002/nbm.2880.

Quantitative analysis of hyperpolarized ^{129}Xe ventilation imaging in healthy volunteers and subjects with chronic obstructive pulmonary disease

Rohan S. Virgincar[1,2,3], **Zackary I. Cleveland**[1,3], **S. Sivaram Kaushik**[1,2], **Matthew S. Freeman**[1,4], **John Nouls**[1,3], **Gary P. Cofer**[1,3], **Santiago Martinez-Jimenez**[3], **Mu He**[1,5], **Monica Kraft**[6], **Jan Wolber**[7,8], **H. Page McAdams**[3], and **Bastiaan Driehuys**[1,2,3,4]

[1]Center for In Vivo Microscopy, Duke University Medical Center, Durham, NC, USA

[2]Department of Biomedical Engineering, Duke University, Durham, NC, USA

[3]Department of Radiology, Duke University Medical Center, Durham, NC, USA

[4]Medical Physics Graduate Program, Duke University, Durham, NC, USA

[5]Department of Electrical and Computer Engineering, Duke University, Durham, NC, USA

[6]Department of Pulmonary and Critical Care Medicine, Duke University Medical Center, Durham, NC, USA

[7]GE Healthcare, The Grove Center, White Lion Rd, Amersham, UK

[8]Academic Radiology, University of Sheffield, Royal Hallamshire Hospital, Sheffield, UK

Abstract

In this study, hyperpolarized (HP) ^{129}Xe MR ventilation and ^{1}H anatomical images were obtained from 3 subject groups: young healthy volunteers (HV), subjects with chronic obstructive pulmonary disease (COPD), and age-matched control subjects (AMC). Ventilation images were quantified by 2 methods: an expert reader-based ventilation defect score percentage (VDS%) and a semi-automatic segmentation-based ventilation defect percentage (VDP). Reader-based values were assigned by two experienced radiologists and resolved by consensus. In the semi-automatic analysis, ^{1}H anatomical images and ^{129}Xe ventilation images were both segmented following registration, to obtain the thoracic cavity volume (TCV) and ventilated volume (VV), respectively, which were then expressed as a ratio to obtain the VDP. Ventilation images were also characterized by generating signal intensity histograms from voxels within the TCV, and heterogeneity was analyzed using the coefficient of variation (CV). The reader-based VDS% correlated strongly with the semi-automatically generated VDP ($r = 0.97$, $p < 0.0001$), and with CV ($r = 0.82$, $p < 0.0001$). Both ^{129}Xe ventilation defect scoring metrics readily separated the 3 groups from one another and correlated significantly with FEV_1 (VDS%: $r = -0.78$, $p = 0.0002$; VDP: $r = -0.79$, $p = 0.0003$; CV: $r = -0.66$, $p = 0.0059$) and other pulmonary function tests. In the healthy subject groups (HV and AMC), the prevalence of ventilation defects also increased with age (VDS%: $r = 0.61$, $p = 0.0002$; VDP: $r = 0.63$, $p = 0.0002$). Moreover, ventilation histograms

---

Correspondence to: Bastiaan Driehuys, Ph.D. Center for In Vivo Microscopy, Box 3302, Duke University Medical Center, Durham, NC 27710 bastiaan.driehuys@duke.edu, Phone: 919-684-7786, Fax: 919-684-7122.

and their associated CVs distinguished between COPD subjects with similar ventilation defect scores but visibly different ventilation patterns.

Keywords

hyperpolarized; ^{129}Xe; Xe-129; magnetic resonance imaging; ventilation; defect; segmentation; COPD; coefficient of variation; VDP; VDS; VDV; FEV1

INTRODUCTION

Chronic obstructive pulmonary disease (COPD) is a leading cause of morbidity and mortality globally and characterized by progressive, irreversible airflow limitation, which is associated with a mixture of abnormal inflammatory responses in small airways (obstructive bronchiolitis) and parenchymal destruction (emphysema) (1). Due to the enormous health burden and poor prognosis for individuals afflicted with COPD, numerous multi-center clinical trials have been performed to test potential COPD therapies. Unfortunately, these trials have failed to identify effective pharmacological treatments, and it is increasingly believed that these failures have occurred, in part, because COPD trials typically define therapeutic outcomes in terms of spirometric pulmonary function tests (PFTs) (2), which have been shown to correlate poorly with patient symptoms (3) and survival (4,5). Moreover, there is a growing consensus that improved diagnostic tools and quantitative metrics must be developed to better classify subject populations (i.e., COPD phenotypes), quantify disease progression, and assess therapeutic responses (6).

To this end, hyperpolarized (HP) ^{3}He, which permits high-resolution imaging of lung function (~$3 \times 3 \times 10$ mm^3) due to its large nuclear magnetic moment and mature polarization technology (7), has emerged as a promising tool for studying and monitoring COPD. In addition to requiring no ionizing radiation and being well tolerated (8), HP ^{3}He can be used to routinely detect emphysematous degeneration of pulmonary microstructure through apparent diffusion coefficient-weighted MR imaging (MRI) (9-11) and, more directly, to visualize regions of obstructed ventilation (12). Furthermore, a variety of ventilation scoring metrics have been developed for assessing ^{3}He MR images, including reader-based scoring (13-15), manual segmentation (12,16-18), semi-automated segmentation (12,19), and fully automated feature analysis (20,21). In addition to quantifying ventilation defects, Tzeng et al. (22) showed ventilation heterogeneity to be an additional useful means of classifying these images. Quantitative HP ^{3}He MRI is sufficiently sensitive to detect reduced ventilation, even in asymptomatic smokers (12), and to reveal lung function decline in COPD subjects, even when spirometric measures of lung function such as forced expiratory volume in 1 second (FEV$_1$) remain constant (23). Moreover, HP ^{3}He was recently used to demonstrate that ventilation improves after bronchodilator administration in COPD patients who were defined as non-responders based on changes in FEV$_1$ (24). Additionally, it has been suggested that, by combining HP ^{3}He ADC and ventilation MR imaging, it may be possible to better classify subjects with COPD into different phenotypes (16).

Unfortunately, despite its enormous promise, HP ^{3}He has failed to achieve widespread clinical use because of its limited global supply. Moreover, even basic research applications will likely be limited in the coming years due to sharply increasing costs resulting from increased security applications, as well as a finite and dwindling ^{3}He stockpile (25). These issues have stimulated a need to transition to ^{129}Xe, which offers a practically unlimited supply. This transition began when Patz et al. introduced the feasibility of ^{129}Xe MRI in humans and obtained encouraging results (26,27). More recently, our group reported results from a Phase I clinical trial for ^{129}Xe MRI, demonstrating that this gas, like HP ^{3}He, is well tolerated (28), and that HP ^{129}Xe ADC imaging can detect emphysematous destruction of the pulmonary parenchyma (29).

An additional objective of this trial was to implement HP ^{129}Xe MR image-based metrics, similar to those used in HP ^{3}He MRI, to quantify ventilation, ventilation defects, and differences in ventilation patterns between subject groups and then to correlate these metrics with pulmonary function tests and demographic information. More specifically, our aim in this study was to develop a semi-automatic segmentation approach that not only readily quantifies ^{129}Xe ventilation defects, but also provides a robust framework for extending ventilation analysis beyond a single defect score. Finally, to provide context and validation for this segmentation, we compare the semi-automated results with an expert reader-based image scoring approach (13).

EXPERIMENTAL

Subjects

Studies were conducted under the GE Healthcare Investigational New Drug (IND) application as part of a Phase I clinical trial for hyperpolarized ^{129}Xe MRI that consisted of a technical run-in phase for pulse sequence development and an efficacy phase involving subjects with COPD. All studies were approved by the Duke University Medical Center Institutional Review Board (IRB), and prior to enrollment, written informed consent was obtained from all subjects. A total of 44 subjects were enrolled: 24 healthy volunteers (HV; 16 female, 8 male; mean age 32.2 ± 11.4 years) in the technical run-in phase; 10 subjects with COPD [3 female, 7 male; mean age 69.5 ± 6.4 years; 9 with GOLD (1) stage II and 1 with GOLD stage III]; and 10 age-matched controls (AMC; 6 female, 4 male; mean age 62.9 ± 7.8 years). Of these 44 subjects, 2 AMC and 2 COPD subjects were excluded from data analysis, because their ventilation images were corrupted due to a malfunctioning ^{129}Xe coil. One HV subject was also excluded from analysis, because no ^{1}H MR image was available to define the thoracic cavity for the semi-automated analysis.

Subjects were excluded from the study if they were pregnant or lactating; had a history of asthma, allergy, or hypersensitivity that affects the pulmonary function; had a history of cardiac arrhythmias; or had a respiratory illness (or exacerbation for COPD subjects) within 30 days of imaging. All subjects with COPD had a smoking history of at least 20 pack-years, while AMC subjects were recruited who had less than 5 pack-years and had not smoked for at least 5 years prior to participating in the study. A list of demographic information and pulmonary function test data (COPD subjects and AMCs only) and a detailed summary of subject demographics are provided in references (28,29).

^{129}Xe Polarization and Delivery

Isotopically enriched ^{129}Xe gas (83% ^{129}Xe, Spectra Gases Inc., Alpha, NJ) was hyperpolarized to 6–10% by rubidium vapor spin-exchange optical pumping and cryogenically accumulated (30) in 1-L doses using a prototype commercial polarizer (GE Healthcare, Durham, NC). HP ^{129}Xe was then thawed into a Tedlar bag (Jensen Inert Products, Coral Springs FL), and the polarization was determined using a prototype polarization measurement station (GE Healthcare). HP ^{129}Xe was administered by first instructing the subjects, who were lying supine in the MR magnet, to exhale to functional residual capacity (FRC) and then inhale the 1-L contents of the Tedlar bag through 0.95-cm inner diameter Tygon tubing (Saint-Gobain Performance Plastics, Akron, OH). Subjects were then instructed to hold their breath for the 8−12-second image acquisition.

MR Imaging

All images were acquired on a 1.5 T GE Healthcare EXCITE 14M5 MR system (GE Healthcare, Waukesha, WI). Subjects were fitted with 17.66-MHz ^{129}Xe quadrature vest coil (Clinical MR Solutions, Brookfield, WI) that was made transparent to RF at the ^{1}H resonance frequency by fitting the ^{129}Xe coil with ^{1}H frequency resonant trap circuits. This configuration permitted shimming and localizing with the scanner's ^{1}H body coil with the subject in the same position as for ^{129}Xe MRI. ^{1}H anatomical images were acquired during a 16-second breath-hold that the subject initiated from FRC without explicit volume control. ^{1}H imaging employed a steady-state free precession (SSFP) sequence (FOV = 40×40 cm^{2}, 192×192 matrix, 15-mm slices, TR/TE = 2.8/1.2 ms, $\alpha = 45°$, BW = 125 kHz). HP ^{129}Xe ventilation images were acquired during a separate 16-second breath-hold, in the anterior-to-posterior direction using a slice-selective, spoiled gradient recalled echo (SPGRE) sequence (FOV = 40×28−40 cm^{2}, 15-mm slices, TR/TE = 7.9/1.9 ms, α = 5–7°, BW = 8.0 kHz). All slices were acquired using 128 frequency-encoding points. For subjects with smaller lungs, the FOV in the phase-encoding direction was reduced (range 28−40 cm) along with the number of phase-encoding steps (range 90–128). When phase-encoding steps could be reduced, the flip angle was commensurately increased (5–7°) to improve SNR. This range of flip angles is slightly below the range (7.1–8.5°) that would have optimized the SNR (i.e., the signal in central line of k-space) for sequentially encoded images (31), but rather it maximized the signal of the final phase encode, thus decreasing imaging blurring caused by RF-induced signal decay, while still providing sufficient SNR for quantitative analysis.

Visual Image Scoring

Images were scored by two board-certified thoracic radiologists (S.M.J. and H.P.M), using a system similar to that proposed by Donnelly et al. (13), and any discrepancy in the scoring was resolved by consensus. The radiologists were not blinded to the subject group, but were blinded to the results of automatic segmentation, described in the following section. The left and right lungs were each divided into 3 regions (apical – lung apex to aortic arch; middle – aortic arch to inferior pulmonary vein; basal – inferior pulmonary vein to diaphragm), and the extent of ventilation defects was scored in each region as: 0 = no defects; 1 = 0–25%; 2 = 25–50%; 3 = 50–75%; and 4 = 75–100%. These scores were summed over all regions to obtain a final ventilation defect score (VDS) for each subject in the range of 0–24. This VDS was then linearly converted to a 0-100 scale and is referred to as percentage ventilation defect score (VDS%). This conversion facilitated comparison with the semi-automated analysis (described next), which also exhibits a range of 0–100.

Image Segmentation

^{129}Xe ventilation and ^{1}H images were segmented by two analysts using a semi-automated approach based on that of Mathew et al. (12,16). Analysts were blinded to the subjects' identity, disease status, and the VDS%. The ^{1}H SSFP images were segmented by a region-growing technique, using 3D Slicer 3.6 (http://www.slicer.org/) to obtain a binary thoracic cavity mask. Region growing was initiated by analysts placing a seed voxel in the lowest intensity areas of the right and left lung in the central slice of the thoracic cavity. Each analyst then defined a multiplier value to specify the number of standard deviations about the intensity of the seed voxel to be included in the segmentation. A scalar threshold range was then calculated using the mean intensity of the seed voxel plus or minus the multiplier value. The algorithm then constructed a volumetric segmentation by labeling all voxels that are connected to the seed voxel and satisfy the scalar threshold range. The accuracy of the segmentation was judged by visual inspection, and, if necessary, the multiplier was adjusted to capture the entire thoracic cavity (and only the thoracic cavity) within the resulting mask.

The initial thoracic cavity segmentation required additional refinement to account for partial volume effects. Specifically, lung regions containing pulmonary vasculature were initially excluded from the thoracic cavity mask (Figure 1f), but those regions frequently exhibited clearly visible ^{129}Xe signal in the ventilation images (Figure 1b). This discrepancy is attributable to small vessels or partial volume overlap of large vessels that exhibited sufficient ^{1}H signal intensity to be excluded from the thoracic cavity mask but that did not occupy the entire 15-mm slice thickness. This problem was resolved by removing these partial volume-related voids in the thoracic cavity mask via a morphological closing operation performed in MATLAB (MathWorks Inc., Natick, MA), using a disk-shaped structuring-element of radius 6 pixels (Figure 1g). This closing operation resulted in masks with TCVs for each subject that were not significantly different from their measured FRC + 1 L ($p = 0.99$) and was used as a reasonable estimate of the lung volume under which the breath-hold SSFP images were acquired. Prior to the closing operation, the TCVs were significantly less than FRC+1 L ($p = 0.0114$).

Because HP ^{129}Xe ventilation images and the SSFP thoracic cavity images were acquired over different breath-holds, they required registration. This was done using an affine transform implemented in ANTS (Advanced Normalization Tools; http://picsl.upenn.edu/ANTS/). To make the registration computationally less intensive and improve accuracy, it was constrained to the area defined by the thoracic cavity mask. The constrained area consisted of the thoracic cavity mask that had been dilated by a ball-shaped structuring-element of radius 1 to ensure that it encompassed the entire region of interest in the moving image. The resulting registration was visually examined and deemed acceptable in 30 of the

39 cases. However, in 9 cases, the breath-hold volume differed substantially between the ^{1}H and ^{129}Xe acquisitions causing different lung shapes—particularly in the apical-basal direction. For these cases, an additional landmark-based registration step was performed with 3D Slicer, using a similarity transform (32) capable of stretching the lungs in the apical-basal direction without requiring non-rigid registration.

Following registration to the thoracic cavity masks, the ^{129}Xe ventilation image was segmented by region growing using 3D Slicer to obtain a binary ventilation mask. To segment the ^{129}Xe images, again one seed voxel was placed in the right and left lung. While this was sufficient for the HV and AMC subjects, the COPD subjects frequently exhibited disconnected ventilated regions and required multiple seeds voxels be placed in one or more slices to ensure all ventilated regions were included in the segmentation. A ventilation defect was defined as a region within the thoracic cavity mask where the signal from the ^{129}Xe ventilation image fell below the threshold set by the analyst.

Using the registered thoracic cavity and ventilation masks, ventilation defect maps and ventilation defect percentages (VDP) were generated in MATLAB. Ventilation masks were first modified to remove the major airways visible in the central 4 image slices by dividing these slices by the corresponding slices of the registered thoracic cavity mask, which delineated only the lung cavity without airways (Note: this step was necessary because the SSFP sequence used to obtain the thoracic cavity mask did not depict the airways due to poor contrast for these tissues). This division by the thoracic mask returned values of infinity for all airway voxels, which were then set to zero. In this revised ventilation mask without airways, the voxels were summed and multiplied by their volumes to calculate the ventilated volume (VV). Similarly, the thoracic cavity volume (TCV) was calculated from the thoracic cavity mask. The ventilation defect volume (VDV) was obtained by subtracting the ventilation volume from the thoracic cavity volume, and the VDV/TCV ratio was used to define the VDP. A flow chart of the complete process is illustrated in Figure 1.

An important aspect of this approach is that once ^{129}Xe ventilation images have been registered to the thoracic cavity, they can be analyzed for additional features, such as ventilation heterogeneity that may better retain the unique spatial information inherent in the images. Histograms were generated from the ^{129}Xe ventilation images using only those pixels falling within the thoracic cavity. Confining the analysis to the thoracic cavity avoided both the need to set an SNR- based threshold, which would have skew the distribution towards high intensities; and prevented noise from outside the lung from being included, which would have skew the distribution towards low intensities. Within the thoracic cavity, voxels in the ventilation image were first normalized by dividing with the average of the highest 5% intensity values to produce a ventilation distribution with a range of approximately 0–1. This normalized distribution was then used to calculate the ventilation image coefficient of variation (CV).

Statistical Analysis

All statistical analysis was done using JMP 9 (SAS Institute Inc., Cary, NC) and MATLAB. Linear regression analysis and the Pearson's correlation coefficient (r) were used to test the correlation of VDS%, VDP, and CV with each other; and with FEV_1, FEV_1/FVC, diffusing capacity (DL_{CO}), DL_{CO} corrected for alveolar volume (DL_{CO}/Va), and subject age. Agreement between reader-based VDS% and semi-automated VDP was further characterized via Bland-Altman analysis. The fixed effects one-way ANOVA test was used to evaluate whether the ventilation defect scoring systems separated the subjects into significantly different groups. Following the ANOVA test, the Wilcoxon's Rank-Sum test was used for pair-wise comparisons of the means of individual groups. The level of significance for these tests after applying a Bonferroni adjustment for the 3 subject groups was 1.67% ($p < 0.0167$). For all other comparisons and correlations, the level of significance was 5% ($p < 0.05$).

For both the ventilation and thoracic cavity masks, linear regression was used to evaluate the inter-user reproducibility of the multiplier values used in the semi-automatic segmentation. Additionally, agreement between the masks generated by both analysts was evaluated by calculating the Dice coefficient (19) and by Bland-Altman analysis.

RESULTS

Ventilation Defect Scoring

Ventilation images were successfully obtained from all 44 subjects (see Figures 2–4) and displayed sufficient SNR to be scored by the expert readers. However, images from 5 of these subjects could not be used for semi-automatic quantification for technical reasons (see EXPERIMENTAL, Subjects). For the remaining subjects, the images were of sufficient quality and displayed sufficiently high SNR to quantify both VDP and VDS%. Moreover, despite variations in image SNR due to differing ^{129}Xe polarization and subject lung volume, no significant SNR-dependence was found for either VDP ($r = 0.09$, $p = 0.60$) or VDS% ($r = 0.10$, $p = 0.55$).

Both VDP and VDS% separated the subjects into three distinct groups ($p < 0.0001$; see Table 1). For instance, most healthy volunteers (see Figure 2) exhibited homogeneous and complete ventilation in all parts of the lung, with the mean VDS% for this group being 3.03 ± 5.17% (range = 0.0–16.7%), and the mean VDP being 2.72 ± 2.39% (range = 0.00–9.23%). Further, even in those HVs who did exhibit some ventilation defects (Figure 2b and c), the ventilation impairment was relatively minor (VDS% < 17% and VDP < 10%). In contrast to the HV group, ventilation defects were more frequent and larger in the older AMC group (see Figure 3). Although two AMC subjects exhibited VDS% = 0.00% (Figure 3a), the mean VDS% for AMCs was 13.0 ± 10.3% (range = 0–25%), which was significantly different from the HVs ($p = 0.0099$). Similarly, the mean VDP for the AMC group was 7.77 ± 5.27% (range = 1.7–15.9%), which was also significantly different from the HVs ($p = 0.007$).

As expected, ventilation defects occurred with greatest frequency and volume in the COPD group (see Figure 4). This group exhibited a mean VDS% of 47.4 ± 11.6% (range = 33.3–66.7%), which was significantly different from both the HV ($p < 0.0001$) and AMC group ($p = 0.0009$). Similarly, the COPD group had a VDP of 24.7 ± 7.6% (range = 13.7–37.2%), which again was significantly different from both the HV ($p < 0.0001$) and AMC groups (p

= 0.0014). Group-wise comparisons of VDS% and VDP for all subjects are shown in Figure 5a.

While both VDS% and VDP statistically separated the 3 subjects from each other, the results for the two methods do differ. Specifically, the mean VDS% values are generally higher and have a greater spread (range = 0.0–66.7%) than the VDP values (range = 0.0–37.2%). Despite these differences, the reader-based VDS% correlated strongly with the semi-automatic segmentation-based VDP ($r = 0.97$, $p < 0.0001$) as shown in Figure 6a. The poorest concordance was seen in subjects within the lower ranges of both VDS% and VDP, and in fact, 15 subjects had a VDS% of 0 but a non-zero VDP. Thus, the strong correlation seen in Figure 6a is driven largely by the subjects with larger ventilation defect volumes.

Ventilation Heterogeneity

Histograms displaying the relative distribution of ventilation within the lungs, along with the corresponding distribution CVs, provide complimentary information to that provided by the ventilation defect metrics. Figure 7a shows sample image slices and normalized ventilation histograms for one AMC subject with low defect scores (VDS% = 8.33% and VDP = 1.78%); three COPD subjects (b-d) with moderate, but similar scores (VDS% range = 46–50%, VDP = 22–29%); and one COPD subject (e) with more severe disease (VDS% = 66.7%, VDP = 37.2%). For the AMC (Figure 7a), the histogram appears normally distributed with a mean near the center of the gray-scale and produces a relatively modest CV of 0.36. In contrast, Figures 7b-e show COPD subjects whose ventilation histograms are notably skewed toward lower gray-scale values with markedly larger CV (0.57–1.2) than that of the AMC subject. Finally, it is interesting to note that images of the COPD subjects with similar VDS% and VDP in Figure 7b-d display substantial differences in CV (0.57–0.84), reflecting disease-associated variations in ventilation heterogeneity among these subjects.

The mean CV for HVs was 0.42 ± 0.08 (range = 0.31–0.64) and for AMCs was 0.45 ± 0.08 (range = 0.35–0.57). These two means were significantly different from that of the COPD group [$p = 0.0003$ (HV) and $p = 0.0024$ (AMC)], which was 0.75 ± 0.26 (range = 0.47–1.18), but not significantly different from each other ($p = 0.34$) (Note: p-values for all group-wise comparisons are provided in Table 1.) Also, as ventilation defect volume increases, the CV also tends to increase, as is seen quantitatively in Figure 6b, where the CV correlated well with VDS% ($r = 0.85$, $p < 0.0001$).

Correlations with Pulmonary Function Testing and Age

VDP correlated well with FEV_1 ($r = -0.79$, $p = 0.0003$; see Figure 8a) and other PFTs, as did VDS% (see Table 2). Among all the PFTs, the highest correlation observed was with DL_{CO} ($r = -0.85$, $p < 0.0001$). Furthermore, for the HV and AMC groups, Figure 8b shows that a significant correlation also exist between VDP and subject age ($r = 0.63$, $p = 0.0002$), and between VDS% and subject age ($r = 0.61$, $p = 0.0002$; see Table 2). CV also demonstrated good correlations with FEV_1 ($r = -0.66$, $p = 0.0059$; see Figure 8c) and other PFTs (see Table 2). The correlation of CV with age, however, was not significant ($r = 0.19$, $p = 0.30$; see Figure 8d).

Inter-observer Variability

Semi-automatic segmentation of both ^{1}H and ^{129}Xe images showed good inter-observer agreement, as assessed by comparing the multiplier values used by each observer to construct the ventilation and thoracic cavity masks. To segment the ^{1}H SSFP images, one observer used an average multiplier of 2.11 ± 0.23 while the other used 2.04 ± 0.20. Similarly, the multiplier used to segment the ^{129}Xe ventilation images was 1.77 ± 0.28 for one observer and 1.81 ± 0.30 for the other. The multiplier values used by both observers were strongly and significantly correlated ($r = 0.83$, $p < 0.0001$ for proton SSFP images; $r = 0.89$, $p < 0.0001$ for ^{129}Xe ventilation images). Additionally Bland-Altman analysis was used to compare multiplier values used by the observers (plots not shown) and returned minimal mean differences of 0.03 ± 0.14 for ventilation images and -0.07 ± 0.14 for proton images. Furthermore, the average Dice coefficient describing overlap of masks generated by both observers was 0.92 ± 0.06 for the ventilation masks, and 0.93 ± 0.06 for the thoracic cavity masks.

DISCUSSION

Comparison of Semi-automated and Reader-based Scoring

Excellent correlation ($r = 0.97$, $p < 0.0001$) was obtained between an expert reader-derived VDS% and a semi-automated voxel-by-voxel calculation of VDP. Although, the methods for assigning VDS and calculating VDP differ, their strong correlation indicates that the semi-automated segmentation successfully identifies and quantifies regions having impaired ventilation. However, group-wise classification of VDS% and VDP for all subjects shows two interesting differences between these approaches. Specifically, as seen in Figure 5a, the automated VDP scores for each group tend to be lower and exhibit a narrower range than the similarly scaled reader VDS%. These differences can also be seen in Figure 6a, which plots VDP against VDS%. While identical results would yield a slope of 1, the observed slope was found to be 0.49.

This difference likely occurs because the VDP employs binary segmentation, and therefore classifies each voxel as either ventilated or unventilated. In contrast, an expert-reader can exploit the complete gray-scale range of the image and thus incorporate additional textural information, such as regions that are partially ventilated, to characterize the images in a more nuanced way. This phenomenon is illustrated in Figure 6c, which shows a Bland-Altman plot comparing reader-based VDS% with semi-automated VDP, and demonstrates that quantity VDS% - VDP increases nearly linear ($r = 0.97$, $p < 0.0001$) with the average of the two values. Further, the plot shows a bias (± SD) of 6.1 ± 10.2 that increases in subjects with more ventilation defects. This analysis supports the notion that the radiologists are able to identify more subtle ventilation defects than the binary segmentation algorithm.

Interestingly, it is not the case that VDS% exceeds VDP in every subject. Fifteen control subjects with only modest defects (see Figures 2a and 3a) exhibited VDS% = 0, but non-zero VDP. The mean VDP of these subjects was, however, very low (1.9 ± 1.7%). This finding suggests that radiologists tend to ignore defects if the defects comprise less than 2%

of the total volume while the semi-automatic algorithm considers every voxel regardless of other context.

Ventilation Heterogeneity

Ventilation heterogeneity, as characterized by the CV of the ventilation image histograms from within the thoracic cavity, provides additional information to that provided by ventilation defect scores alone. As shown in Figure 5b, a group-wise comparison of ventilation heterogeneity for the three subject groups reveals that the COPD subjects have the widest range of CVs—a trend similar to that seen for VDS% and VDP (Figure 5a). Also, as seen in Figure 6b, the ventilation CV increased significantly with VDS% ($r = 0.85$, $p < 0.0001$).

Perhaps most interesting is the way in which CV appears to distinguish variations in the ventilation patterns of subjects who exhibit nearly identical VDS% and VDP (subjects in Figures 7b-d). The COPD subject in Figure 7b has a VDP of 23% and exhibits a CV of 0.57, which was higher than that of the AMC in Figure 7a, but lower than that of other COPD subjects with similar VDP (Figure 7b and 7c). Further inspection reveals that the VDP in this subject is dominated by two large emphysematous bullae in the apices of the lung, but the rest of the lung appears homogeneously ventilated. These trends appear to portray the visually perceived differences in ventilation patterns and suggest that such a masked histogram analysis accounts for aspects of the underlying texture of these images, and therefore may have the potential to identify different COPD phenotypes (16).

Correlation of Ventilation Defects with Pulmonary Function Testing and Age

The correlations of ^{129}Xe VDP and VDS% with FEV_1 ($r = -0.79$, $p = 0.0003$; and $r = -0.80$, $p = 0.0002$, respectively) were stronger than the correlations previously reported between ^{3}He ventilation defect volume and FEV_1 ($r = -0.58$) by Mathew et al. (16). Our correlation of VDP with age ($r = 0.63$, $p = 0.0002$) was comparable to the correlation of mean parenchymal ^{129}Xe ADC with age ($r = 0.56$) in a group of HV and AMC, which was recently reported by Kaushik et al. (29) in the same patient population. Such similarities may suggest that the aging process leads, in some individuals, to airspace enlargement, which in turn impairs regional ventilation.

The observation of ventilation defects in healthy subjects and our finding that the magnitude of these defects correlate with age agrees with the work of Parraga et al. (18), who previously reported ventilation defects in healthy elderly volunteers using ^{3}He MRI. However, Parraga et al. found no defects in healthy, middle-aged (44 ± 10 yr) volunteers. In contrast, ^{129}Xe MRI revealed ventilation defects in all age groups and in subjects as young as 23 years old. Furthermore, a significant correlation of both VDP and VDS% with age was observed. While the origin of this discrepancy was not investigated, these observations suggest that the differences may result from the physical nature of the two gases. That is, ^{129}Xe is 43-fold more dense than ^{3}He, and is expected to generate a 43-fold greater resistance to flow under turbulent flow conditions (33). Our hypothesis is also supported by earlier work that directly compared ^{3}He MRI and ^{81m}Kr single photon emission tomography (SPECT) and demonstrated that images based on the 27-fold denser ^{81m}Kr yielded significantly higher ventilation scores than did ^{3}He (34). In general, heavier gases may be able to highlight modest airflow obstruction more effectively than ^{3}He, which through its higher diffusivity, can still reach regions having impaired ventilation (35).

Unlike VDP, CV correlated very poorly with age. This suggests that age-related ventilation defects may not be as heterogeneous as pathological ventilation abnormalities related to COPD. In fact, defects in older subjects tended to be in the lung periphery (18). This idea is further reinforced by a lack of significant difference ($p = 0.34$) found between the mean CVs of the HV and AMC groups.

Semi-automatic Segmentation

Although the semi-automated segmentation has limitations, it does have a number of advantages over both reader scoring and manual segmentation. In the case of manual segmentation, the user is required to make many judgments regarding what constitutes a ventilation defect is and what does not as he or she traces the lung image. Whereas in semi-automated segmentation, the operator makes only a single judgment as to a single threshold (within a constrained bounds) that appears to best capture the difference between ventilated and un-ventilated portions of the image. This method requires only limited user intervention with an analyst specifying seed voxels for region growing, inspecting the resulting segmentation, and slightly adjusting the multiplier parameter as needed. But these steps are quite rapid compared to approaches requiring the analyst to trace the lung's boundaries in all slices. The semi-automatic segmentation process is also robust against inter-observer variability as demonstrated by two metrics: 1) the excellent spatial overlap of the thoracic cavity and ventilation masks generated, and 2) the good agreement between segmentation multipliers employed by the two analysts.

However, additional time is required to transfer images between segmentation, registration, and image analysis packages. As a result, the entire semi-automated process for generating the VDP and CV requires approximately 10 minutes per data set, compared to 1 minute for an expert reader. Fortunately, these processing steps can in principle be further automated, leading to decreased analysis time and improved objectively. Moreover, registration of the ^{129}Xe images to a segmented thoracic cavity mask opens up possibilities for analysis beyond a simple defect score as illustrated here by the heterogeneity analysis.

Study Limitations

User interventions in the segmentation process, while currently necessary, may have introduced a degree of subjectivity to the quantitative ventilation analysis. Thus, it is desirable to develop a segmentation process that automatically places seed points and chooses a suitable multiplier depending on the image SNR. Additional improvements would include extending the analysis to quantify regions of hyperintense and hypointense pixel intensity (19), and correcting for B_1 inhomogeneity (20)—a disadvantage of the flexible vest coil used in this work—and other forms of image bias. Moreover, the process of visually evaluating registration results could be replaced by reporting changes in mutual information, or calculating Dice coefficients. Alternatively, an almost ideal solution for defining the thoracic cavity would be to eliminate image registration entirely, and simultaneously acquire ^{1}H and HP gas ventilation images within a single held breath, as was recently demonstrated by Wild et al. (36).

Another clear limitation of this study is its relatively modest sample size—especially for the AMC and COPD subjects groups. Moreover, the effective sample size was further reduced, because data from 1 HV, 2 AMC, and 2 COPD subjects could not be analyzed for technical reasons. Additionally, no pulmonary function testing was performed for the HV group, preventing the inclusion of imaging data from these subjects in the PFT correlations.

A further limitation of this study was that no attempt was made to normalize the inhaled ^{129}Xe volume or the volume at which the ^{1}H anatomical images were obtained, with respect to the total lung volume of the individual subjects. It is conceivable that the inhaled volume of ^{129}Xe (or air in the case of the ^{1}H anatomical image) might have some influence on the observed VDS%, VDP, and ventilation CV. If so, these variations would be expected to reduce the level of correlation between these metrics and with the subjects' PFTs.

CONCLUSIONS

Despite some technical limitations, the results of this study are promising, and illustrate the potential utility of ^{129}Xe for the imaging of pulmonary ventilation. The ^{129}Xeimages were of sufficient quality to be quantified by both expert-readers and semi-automated segmentation. The strong correlation between these two methods is encouraging and suggests that the semi-automated segmentation captured the core aspects of impaired ventilation observed by the expert readers. Additionally, registration of the ^{129}Xe images to the thoracic cavity image provides an opportunity to identify additional phenotypic markers, as illustrated by CV values, which may distinguish COPD subjects with similar ventilation defect scores but different image character. Moreover, these results tentatively suggest that the high density of ^{129}Xe makes it more sensitive to ventilation impairment than ^{3}He. The quantitative techniques developed for assessing impaired pulmonary function will be applicable beyond COPD to other conditions, including asthma (20,37) and cystic fibrosis (13,14,38). Furthermore, these methods are likely to be useful for analyzing images of ^{129}Xe alveolar-capillary transfer and regional gas exchange heterogeneity (39,40).

Acknowledgments

This study was funded by GE Healthcare, with additional support from the Duke Center for In Vivo Microscopy, an NIH/NCRR/NIBIB national Biomedical Technology Resource Center (P41 EB015897), NHLBI R01HL105643, and NCRR UL1 RR024128. The authors also wish to thank Jerry Dahlke of GE Healthcare for assistance with the MR hardware; Sean Fain of the University of Wisconsin-Madison, for supplying the SPGRE sequence used in this work; Christine Willis, Gregory M. Metz, and Rafael Firszt for subject monitoring; Denise M. Beaver for subject recruitment; Kevin T. Kelly for performing ^{1}H MR imaging; Cecil Charles of the Duke Image Analysis Laboratory (DIAL), for valuable discussions regarding image analysis methods; Alexandra Badea for guidance in image registration; and Sally Zimney for carefully proofreading this manuscript.

REFERENCES

1. Rabe KF, Hurd S, Anzueto A, Barnes PJ, Buist SA, Calverley P, Fukuchi Y, Jenkins C, Rodriguez-Roisin R, van Weel C, Zielinski J. Global strategy for the diagnosis, management, and prevention of chronic obstructive pulmonary disease - GOLD executive summary. American Journal of Respiratory and Critical Care Medicine. 2007; 176(6):532–555. [PubMed: 17507545]

2. Cazzola M, MacNee W, Martinez FJ, Rabe KF, Franciosi LG, Barnes PJ, Brusasco V, Burge PS, Calverley PMA, Celli BR, Jones PW, Mahler DA, Make B, Miravitiles M, Page CP, Palange P, Parr D, Pistolesi M, Rennard SI, Molken M, Stockley R, Sullivan SD, Wedzicha JA, Wouters EF. Outcomes for COPD pharmacological trials: from lung function to biomarkers. European Respiratory Journal. 2008; 31(2):416–468. [PubMed: 18238951]
3. Mahler DA, Mackowiak JI. Evaluation of the short-form 36-item questionnaire to measure health-related quality-of-life in patients with COPD. Chest. 1995; 107(6):1585–1589. [PubMed: 7781351]
4. Nishimura K, Izumi T, Tsukino M, Oga T, Japan KCRRG. Dyspnea is a better predictor of 5-year survival than airway obstruction in patients with COPD. Chest. 2002; 121(5):1434–1440. [PubMed: 12006425]
5. Ashutosh K, Haldipur C, Boucher ML. Clinical and personality profiles and survival in patients with COPD. Chest. 1997; 111(1):95–98. [PubMed: 8995999]
6. Han MK, Agusti A, Calverley PM, Celli BR, Criner G, Curtis JL, Fabbri LM, Goldin JG, Jones PW, Macnee W, Make BJ, Rabe KF, Rennard SI, Sciurba FC, Silverman EK, Vestbo J, Washko GR, Wouters EF, Martinez FJ. Chronic obstructive pulmonary disease phenotypes: The future of COPD. American Journal of Respiratory and Critical Care Medicine. 2010; 182(5):598–604. [PubMed: 20522794]
7. Moller HE, Chen XJ, Saam B, Hagspiel KD, Johnson GA, Altes TA, de Lange EE, Kauczor HU. MRI of the lungs using hyperpolarized noble gases. Magnetic Resonance In Medicine. 2002; 47(6): 1029–1051. [PubMed: 12111949]
8. Lutey BA, Lefrak SS, Woods JC, Tanoli T, Quirk JD, Bashir A, Yablonskiy DA, Conradi MS, Bartel ST, Pilgram TK, Cooper JD, Gierada DS. Hyperpolarized He-3 MR imaging: Physiologic monitoring observations and safety considerations in 100 consecutive subjects. Radiology. 2008; 248(2):655–661. [PubMed: 18641256]
9. Salerno M, de Lange EE, Altes TA, Truwit JD, Brookeman JR, Mugler JP. Emphysema: Hyperpolarized Helium 3 diffusion MR imaging of the lungs compared with spirometric indexes—Initial experience. Radiology. 2002; 222(1):252–260. [PubMed: 11756734]
10. Woods JC, Choong CK, Yablonskiy DA, Bentley J, Wong J, Pierce JA, Cooper JD, Macklem PT, Conradi MS, Hogg JC. Hyperpolarized ^{3}He diffusion MRI and histology in pulmonary emphysema. Magnetic Resonance in Medicine. 2006; 56(6):1293–1300. [PubMed: 17058206]
11. Fain SB, Panth SR, Evans MD, Wentland AL, Holmes JH, Korosec FR, O'Brien MJ, Fountaine H, Grist TM. Early emphysematous changes in asymptomatic smokers: Detection with ^{3}He MR imaging. Radiology. 2006; 239(3):875–883. [PubMed: 16714465]
12. Woodhouse N, Wild JM, Paley MNJ, Fichele S, Said Z, Swift AJ, van Beek EJR. Combined helium-3/proton magnetic resonance imaging measurement of ventilated lung volumes in smokers compared to never-smokers. Journal Of Magnetic Resonance Imaging. 2005; 21(4):365–369. [PubMed: 15779032]
13. Donnelly LF, MacFall JR, McAdams HP, Majure JM, Smith J, Frush DP, Bogonad P, Charles HC, Ravin CE. Cystic fibrosis: Combined hyperpolarized ^{3}He-enhanced and conventional proton MR imaging in the lung—Preliminary observations. Radiology. 1999; 212(3):885–889. [PubMed: 10478261]
14. McMahon CJ, Dodd JD, Hill C, Woodhouse N, Wild JM, Fichele S, Gallagher CG, Skehan SJ, van Beek EJR, Masterson JB. Hyperpolarized ^{3}helium magnetic resonance ventilation imaging of the lung in cystic fibrosis: comparison with high resolution CT and spirometry. European Radiology. 2006; 16(11):2483–2490. [PubMed: 16871384]
15. de Lange EE, Altes TA, Patrie JT, Gaare JD, Knake JJ, Mugler JP, Platts-Mills TA. Evaluation of asthma with hyperpolarized helium-3 MRI: correlation with clinical severity and spirometry. Chest. 2006; 130(4):1055–1062. [PubMed: 17035438]
16. Mathew L, Kirby M, Etemad-Rezai R, Wheatley A, McCormack DG, Parraga G. Hyperpolarized ^{3}He magnetic resonance imaging: Preliminary evaluation of phenotyping potential in chronic obstructive pulmonary disease. European Journal of Radiology. 2011; 79(1):140–146. [PubMed: 19932577]
17. Mathew L, Evans A, Ouriadov A, Etemad-Rezai R, Fogel R, Santyr G, McCormack DG, Parraga G. Hyperpolarized ^{3}He magnetic resonance imaging of chronic obstructive pulmonary disease: Reproducibility at 3.0 tesla. Academic Radiology. 2008; 15(10):1298–1311. [PubMed: 18790402]

18. Parraga G, Mathew L, Etemad-Rezai R, McCormack DG, Santyr GE. Hyperpolarized ^{3}He magnetic resonance imaging of ventilation defects in healthy elderly volunteers: Initial findings at 3.0 Tesla. Academic Radiology. 2008; 15(6):776–785. [PubMed: 18486013]
19. Kirby M, Heydarian M, Svenningsen S, Wheatley A, McCormack DG, Etemad-Rezai R, Parraga G. Hyperpolarized ^{3}He magnetic resonance functional imaging semiautomated segmentation. Academic radiology. 2012; 19(2):141–152. [PubMed: 22104288]
20. Tustison NJ, Altes TA, Song G, de Lange EE, Mugler JP III, Gee JC. Feature analysis of hyperpolarized helium-3 pulmonary MRI: A study of asthmatics versus nonasthmatics. Magnetic Resonance in Medicine. 2010; 63(6):1448–1455. [PubMed: 20512846]
21. Tustison NJ, Avants BB, Flors L, Altes TA, de lange EE, Mugler JP III, Gee JC. Ventilation-Based Segmentation of the Lungs Using Hyperpolarized He-3 MRI. Journal of Magnetic Resonance Imaging. 2011; 34(4):831–841. [PubMed: 21837781]
22. Tzeng YS, Lutchen K, Albert M. The difference in ventilation heterogeneity between asthmatic and healthy subjects quantified using hyperpolarized ^{3}He MRI. Journal of Applied Physiology. 2009; 106(3):813–822. [PubMed: 19023025]
23. Kirby M, Mathew L, Wheatley A, Santyr GE, McCormack DG, Parraga G. Chronic obstructive pulmonary disease: Longitudinal hyperpolarized ^{3}He MR Imaging. Radiology. 256(1):280–289. [PubMed: 20574101]
24. Kirby M, Mathew L, Heydarian M, Etemad-Rezai R, McCormack DG, Parraga G. Chronic obstructive pulmonary disease: Quantification of bronchodilator effects by using hyperpolarized ^{3}He MR Imaging. Radiology. 2011; 261(1):283–292. [PubMed: 21813741]
25. Kramer D. DOE begins rationing helium-3. Physics Today. 2010; 63:6.
26. Patz S, Hersman FW, Muradian I, Hrovat MI, Ruset IC, Ketel S, Jacobson F, Topulos GP, Hatabu H, Butler JP. Hyperpolarized ^{129}Xe MRI: A viable functional lung imaging modality? European Journal of Radiology. 2007; 64:335–344. [PubMed: 17890035]
27. Patz S, Muradian I, Hrovat MI, Ruset IC, Topulos G, Covrig SD, Frederick E, Hatabu H, Hersman FW, Butler JP. Human pulmonary imaging and spectroscopy with hyperpolarized ^{129}Xe at 0.2T. Academic Radiology. 2008; 15(6):713–727. [PubMed: 18486008]
28. Driehuys B, Martinez-Jimenez S, Cleveland ZI, Metz GM, Beaver DM, Nouls JC, Kaushik SS, Firszt R, Willis C, Kelly KT, Wolber J, Kraft M, McAdams HP. Chronic obstructive pulmonary disease: Safety and tolerability of hyperpolarized ^{129}Xe MR imaging in healthy volunteers and patients. Radiology. 2012; 262(1):279–289. [PubMed: 22056683]
29. Kaushik SS, Cleveland ZI, Cofer GP, Metz G, Beaver D, Nouls J, Kraft M, Auffermann W, Wolber J, McAdams HP, Driehuys B. Diffusion-weighted hyperpolarized ^{129}Xe MRI in healthy volunteers and subjects with chronic obstructive pulmonary disease. Magnetic Resonance in Medicine. 2011; 65(4):1154–1165. [PubMed: 21413080]
30. Driehuys B, Cates GD, Miron E, Sauer K, Walter DK, Happer W. High-volume production of laser-polarized ^{129}Xe. Applied Physics Letters. 1996; 69(12):1668–1670.
31. Miller GW, Altes TA, Brookeman JR, de Lange EE, Mugler JP. Hyperpolarized ^{3}He lung ventilation imaging with B-1-inhomogeneity correction in a single breath-hold scan. Magnetic Resonance Materials in Physics Biology and Medicine. 2004; 16(5):218–226.
32. Horn BKP. Closed-form solution of absolute orientation using unit quaternions. Journal of the Optical Society of America A. 1987; 4(4):629–642.
33. Drazen JM, Loring SH, Ingram RH. Distribution of pulmonary resistance: effects of gas-density, viscosity, and flow rate. Journal of Applied Physiology. 1976; 41(3):388–395. [PubMed: 965308]
34. Stavngaard T, SoVaard L, Mortensen J, Hanson LG, Schmiedeskamp J, Berthelsen AK, Dirksen A. Hyperpolarised ^{3}He MRI and ^{81m}Kr SPECT in chronic obstructive pulmonary disease. European Journal of Nuclear Medicine and Molecular Imaging. 2005; 32(4):448–457. [PubMed: 15821964]
35. Marshall H, Deppe MH, Parra-Robles J, Hillis S, Billings CG, Rajaram S, Swift A, Miller SR, Watson JH, Wolber J, Lipson DA, Lawson R, Wild JM. Direct visualisation of collateral ventilation in COPD with hyperpolarised gas MRI. Thorax. 2012; 67(7):613–617. [PubMed: 22286930]
36. Wild JM, Ajraoui S, Deppe MH, Parnell SR, Marshall H, Parra-Robles J, Ireland RH. Synchronous acquisition of hyperpolarised ^{3}He and ^{1}H MR images of the lungs - maximising mutual

anatomical and functional information. NMR in Biomedicine. 2011; 24(2):130–134. [PubMed: 20821726]

37. Campana L, Kenyon J, Zhalehdoust-Sani S, Tzeng Y-S, Sun Y, Albert M, Lutchen KR. Probing airway conditions governing ventilation defects in asthma via hyperpolarized MRI image functional modeling. Journal of Applied Physiology. 2009; 106(4):1293–1300. [PubMed: 19213937]
38. Woodhouse N, Wild JM, van Beek EJR, Hoggard N, Barker N, Taylor CJ. Assessment of hyperpolarized ^{3}He Lung MRI for regional evaluation of interventional therapy: A pilot study in pediatric cystic fibrosis. Journal of Magnetic Resonance Imaging. 2009; 30(5):981–988. [PubMed: 19856418]
39. Cleveland ZI, Cofer GP, Metz G, Beaver D, Nouls J, Kaushik SS, Kraft M, Wolber J, Kelly KT, McAdams HP, Driehuys B. Hyperpolarized ^{129}Xe MR imaging of alveolar gas uptake in humans. PLoS ONE. 2010; 5(8):e12192. [PubMed: 20808950]
40. Mugler JP III, Altes TA, Ruset IC, Dregely IM, Mata JF, Miller GW, Ketel S, Ketel J, Hersman FW, Ruppert K. Simultaneous magnetic resonance imaging of ventilation distribution and gas uptake in the human lung using hyperpolarized xenon-129. Proceedings of the National Academy of Sciences of the United States of America. 2010; 107(50):21707–21712. [PubMed: 21098267]

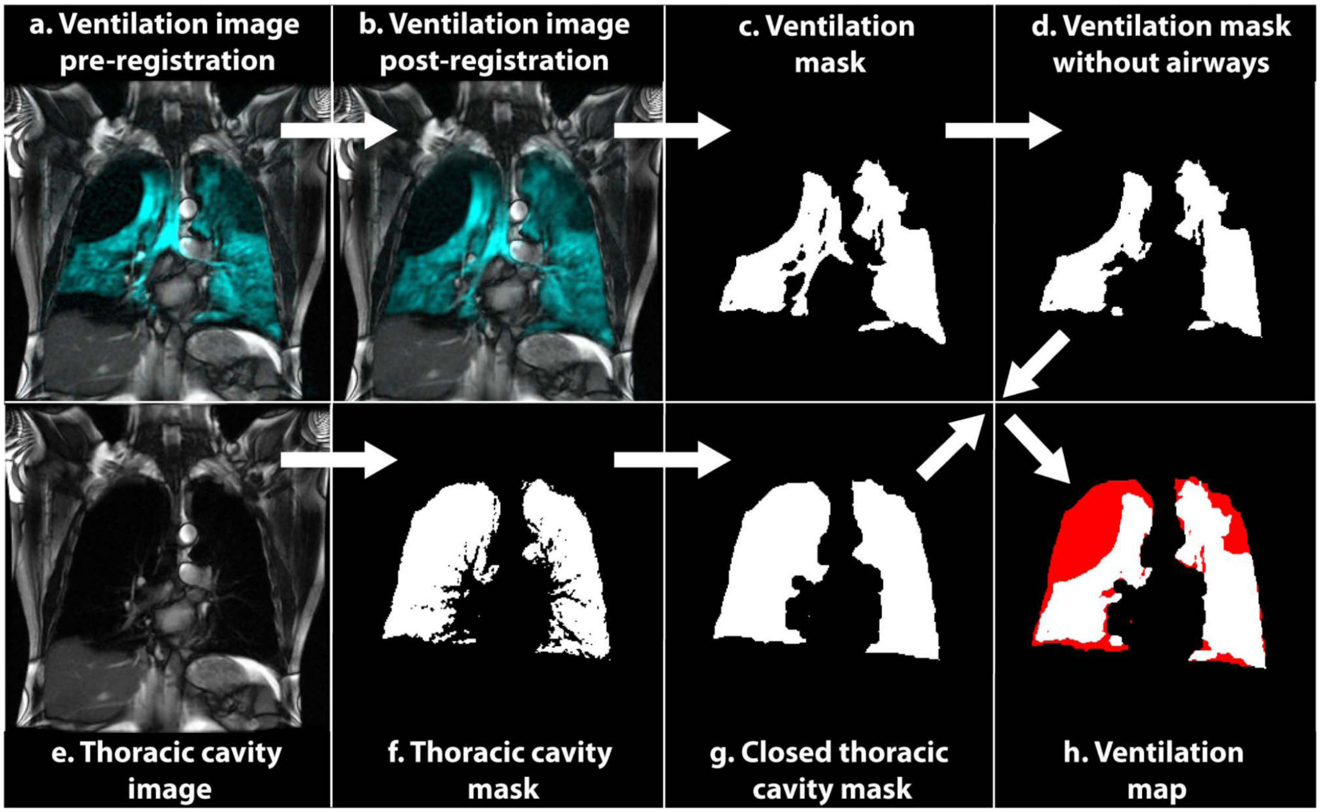

Figure 1.

Semi-automated analysis flowchart. Original ^{129}Xe ventilation images (a) were registered to the ^{1}H SSFP images (b), and then segmented to obtain an initial ventilation mask (c). Airways were removed from (c) to obtain the final ventilation mask (d) from which the ventilated volume (VV) was calculated. Original ^{1}H SSFP anatomical images (e) were segmented to obtain an initial thoracic cavity mask (f). This mask was morphologically closed to obtain the final thoracic cavity mask (g) from which the thoracic cavity volume (TCV) was calculated. VV (white) and TCV (red) were then combined to map ventilation defects (h).

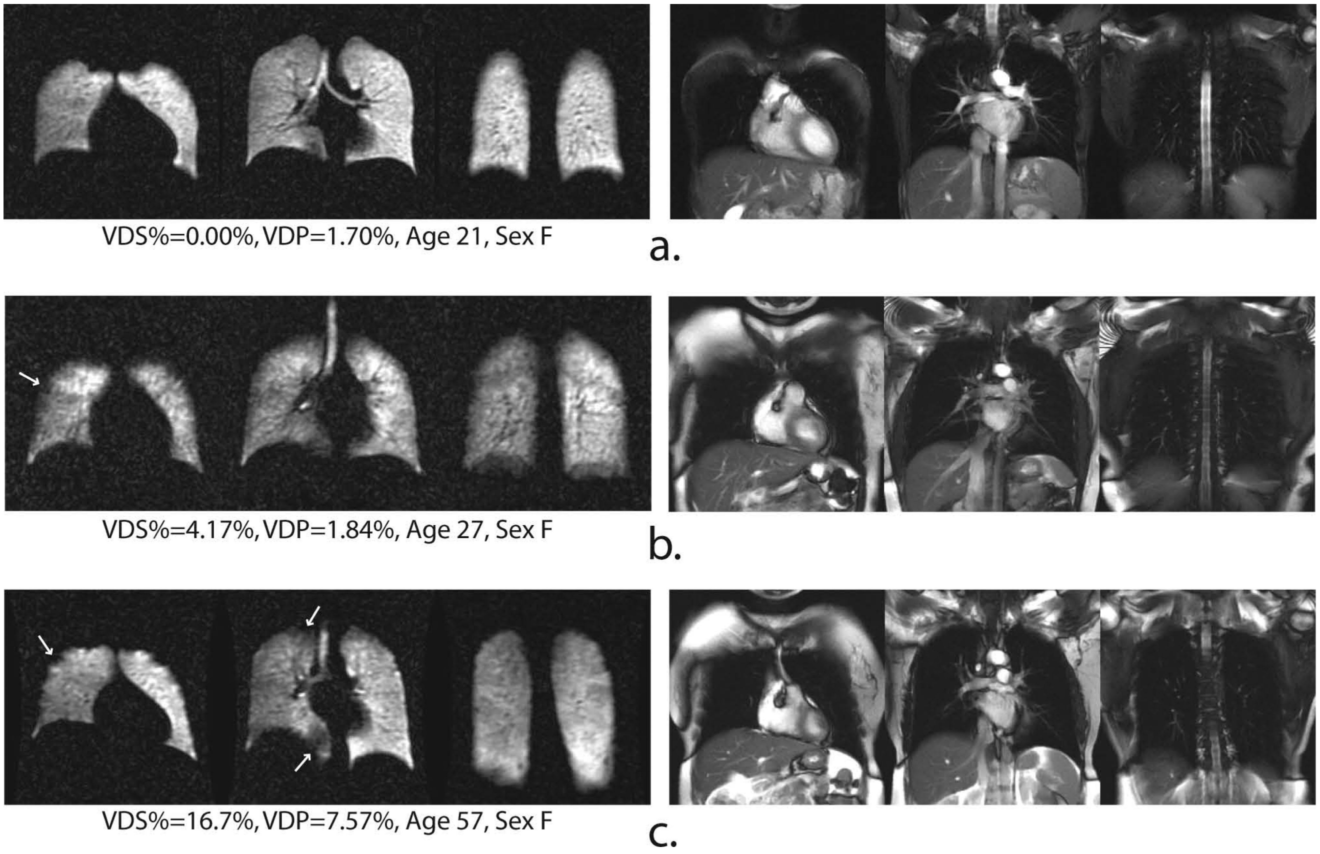

Figure 2.

Representative ^{129}Xe ventilation (left) and ^{1}H SSFP anatomical image (right) slices of three healthy volunteers. Arrows identify small ventilation defects that sometimes observed even in healthy subjects.

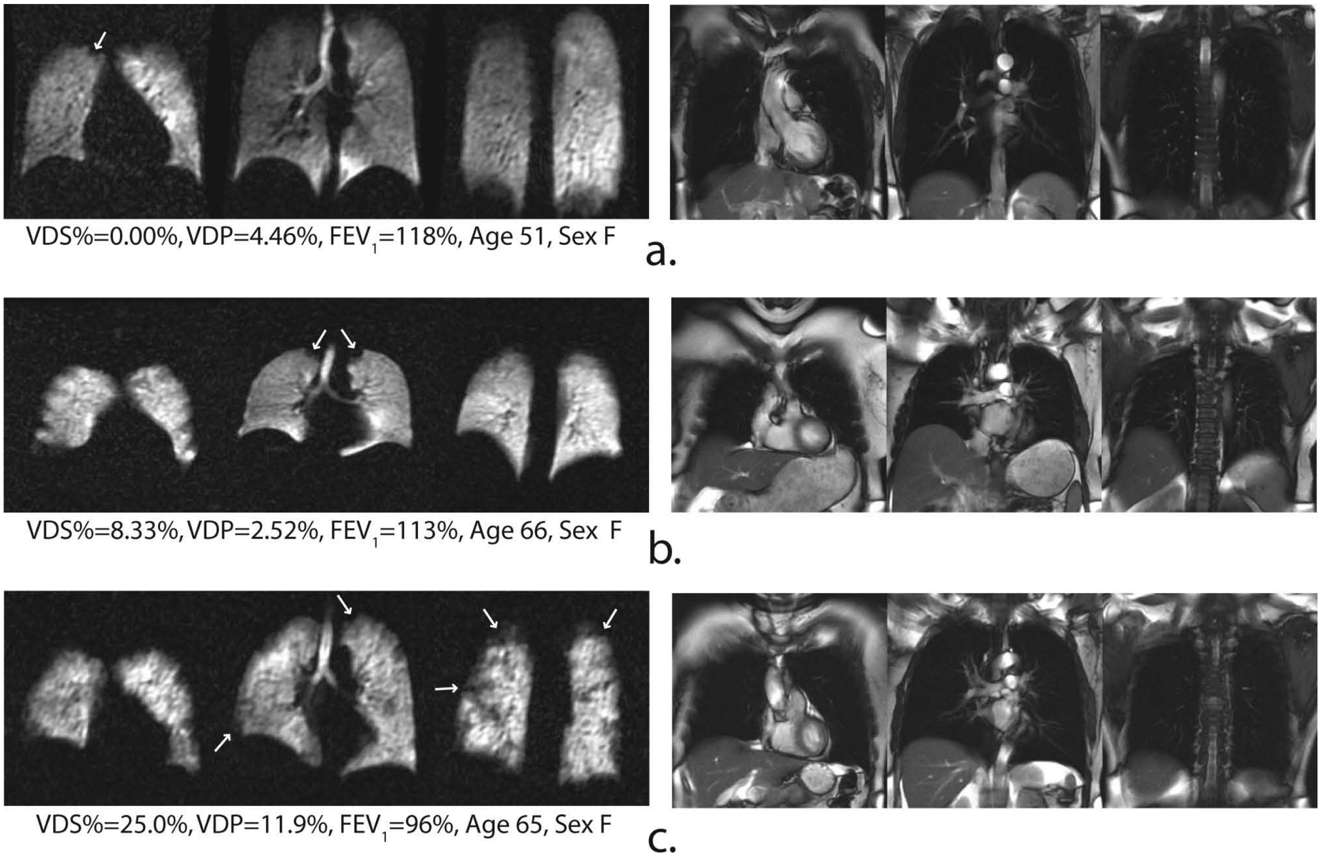

Figure 3.

Representative ^{129}Xe ventilation (left) and ^{1}H SSFP anatomical image (right) slices of three age-matched control subjects. Arrows identify small ventilation defects that sometimes observed even in healthy subjects.

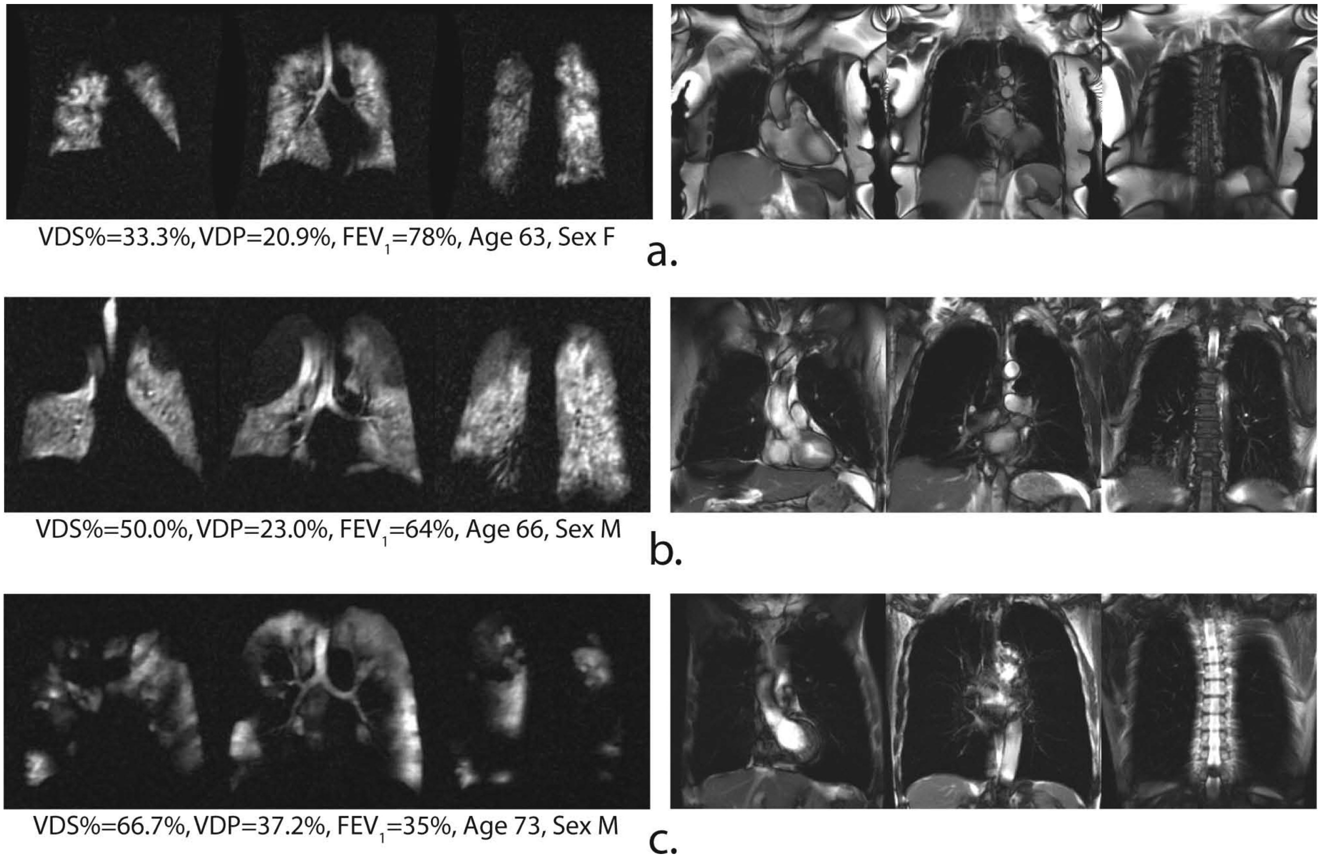

Figure 4.

Representative ^{129}Xe ventilation (left) and ^{1}H SSFP anatomical image (right) slices of three COPD subjects. Note, a variety of ventilation defects are observed throughout the lungs.

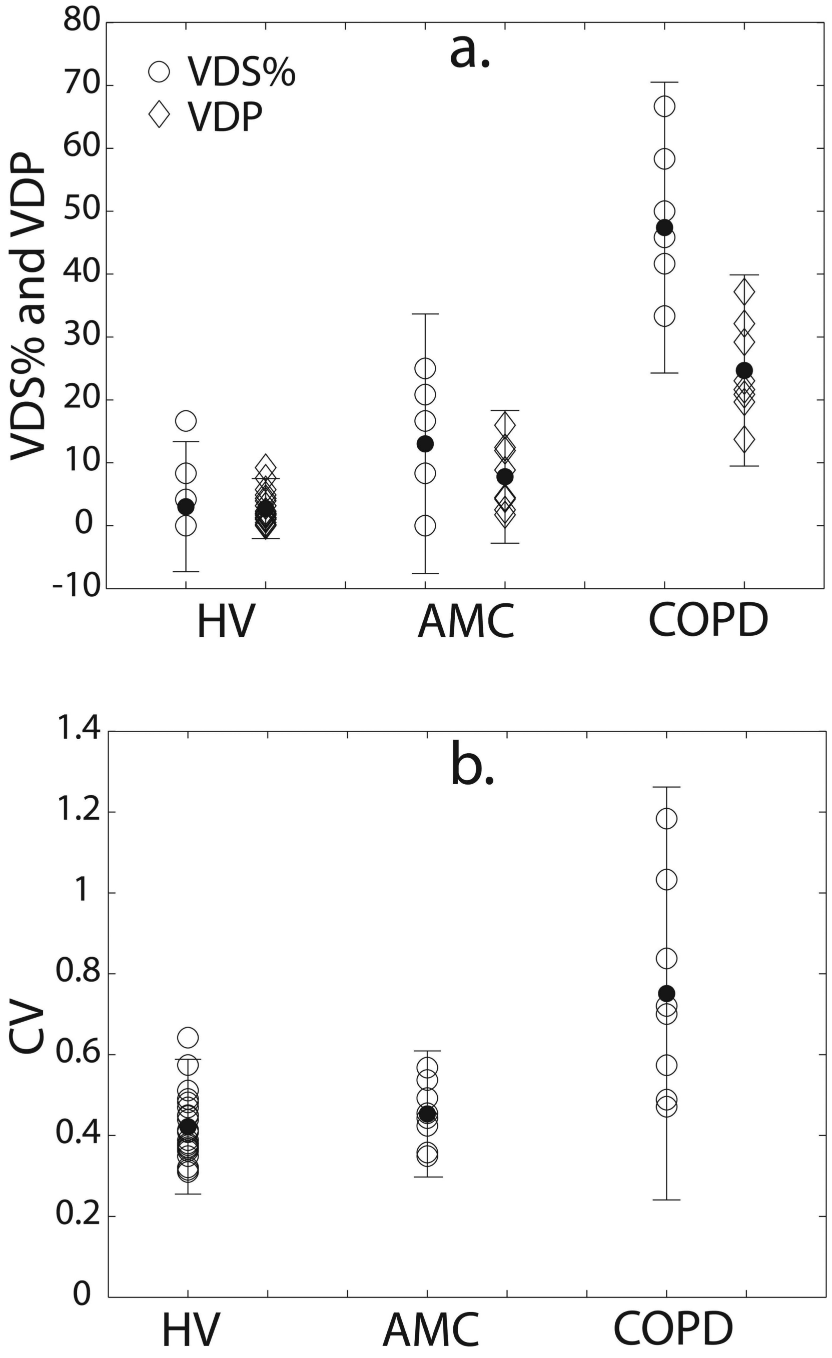

Figure 5.

Group-wise comparison of (a) VDS% and VDP (b) CV for all subjects (open symbols). Error bars are 95% confidence intervals about the group mean (closed symbols). For VDS% and VPD, all groups are significantly different from one another. For CV, the HV and AMC groups are significantly different from the COPD group but not from each other. P-values for all comparisons are provided in Table 1.

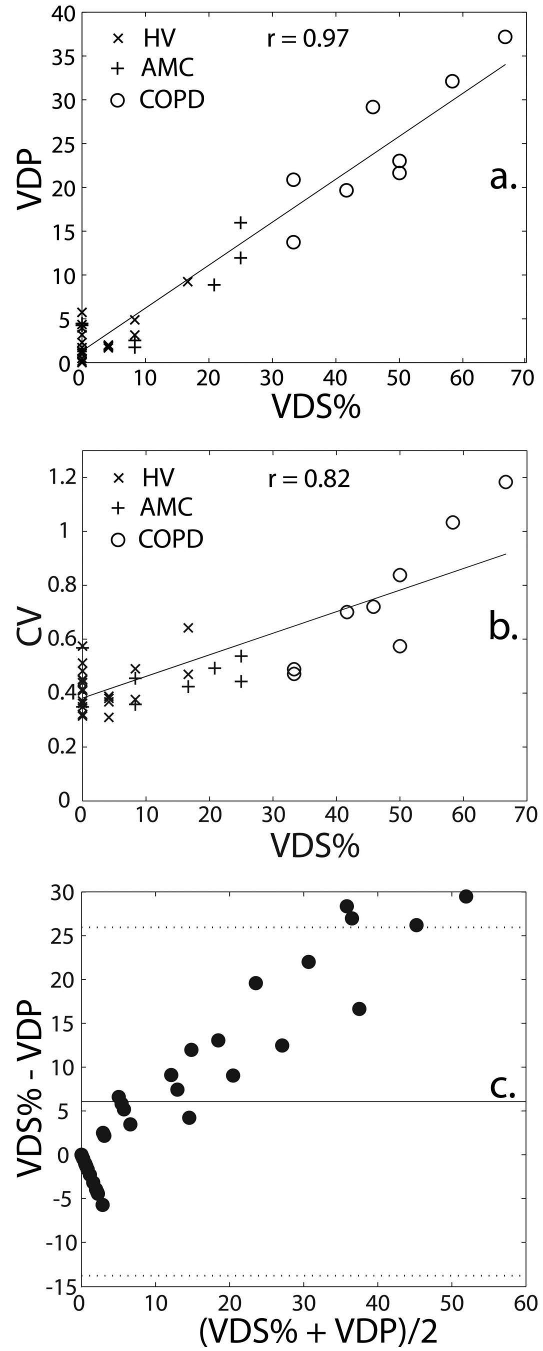

Figure 6.

Correlation of the expert reader-based VDS% with (a) VDP [VDP = 0.49×VDS% + 1.30; $R^2 = 0.94$; $p < 0.0001$] and (b) CV [CV = 0.008×VDS% + 0.382; $R^2 = 0.68$; $p < 0.0001$]; (c) Bland-Altman plot for VDS% and VDP for all subjects. The solid line indicates the mean difference between VDS% and VDP (6.07 ± 10.15) and the dotted lines indicate 95% limits of agreement (lower limit: -13.8, upper limit: 26.0).

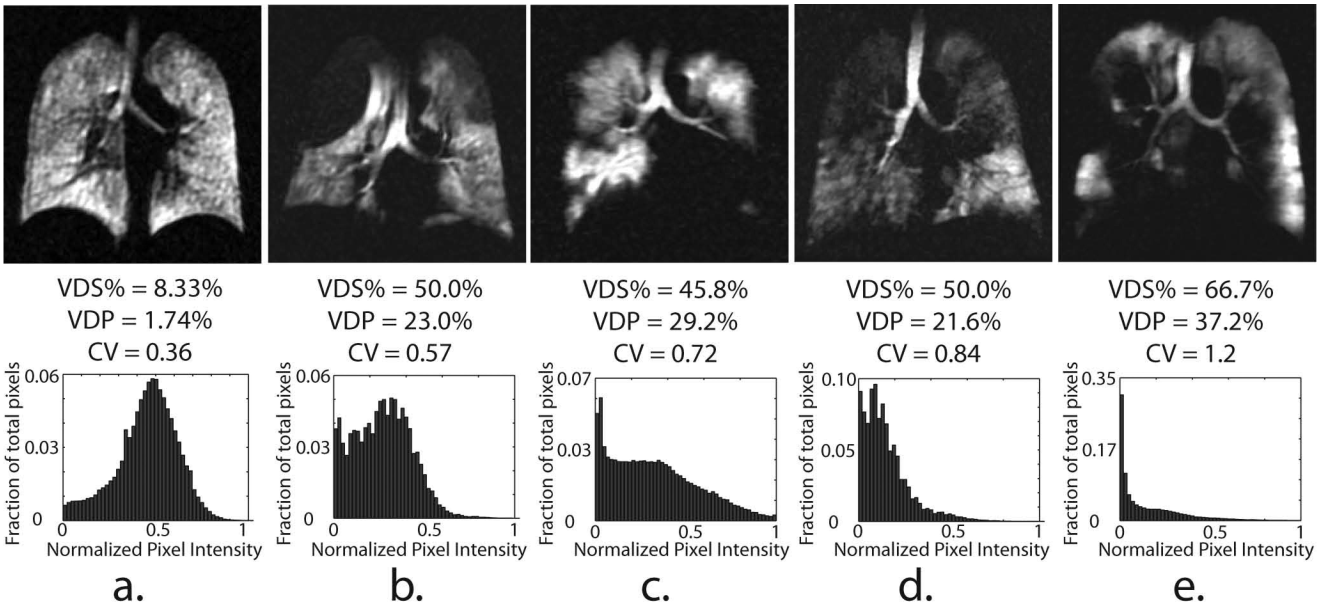

Figure 7.

Representative central slices of ^{129}Xe ventilation images (upper panel) and normalized, whole-lung histograms (lower panel) from a HV (a) and 4 COPD subjects (b-e) ranked in increasing order of the CV. Note, subjects b-e have a similar VDS% (45-50), and VDP (21-23%) but markedly different histograms shapes.

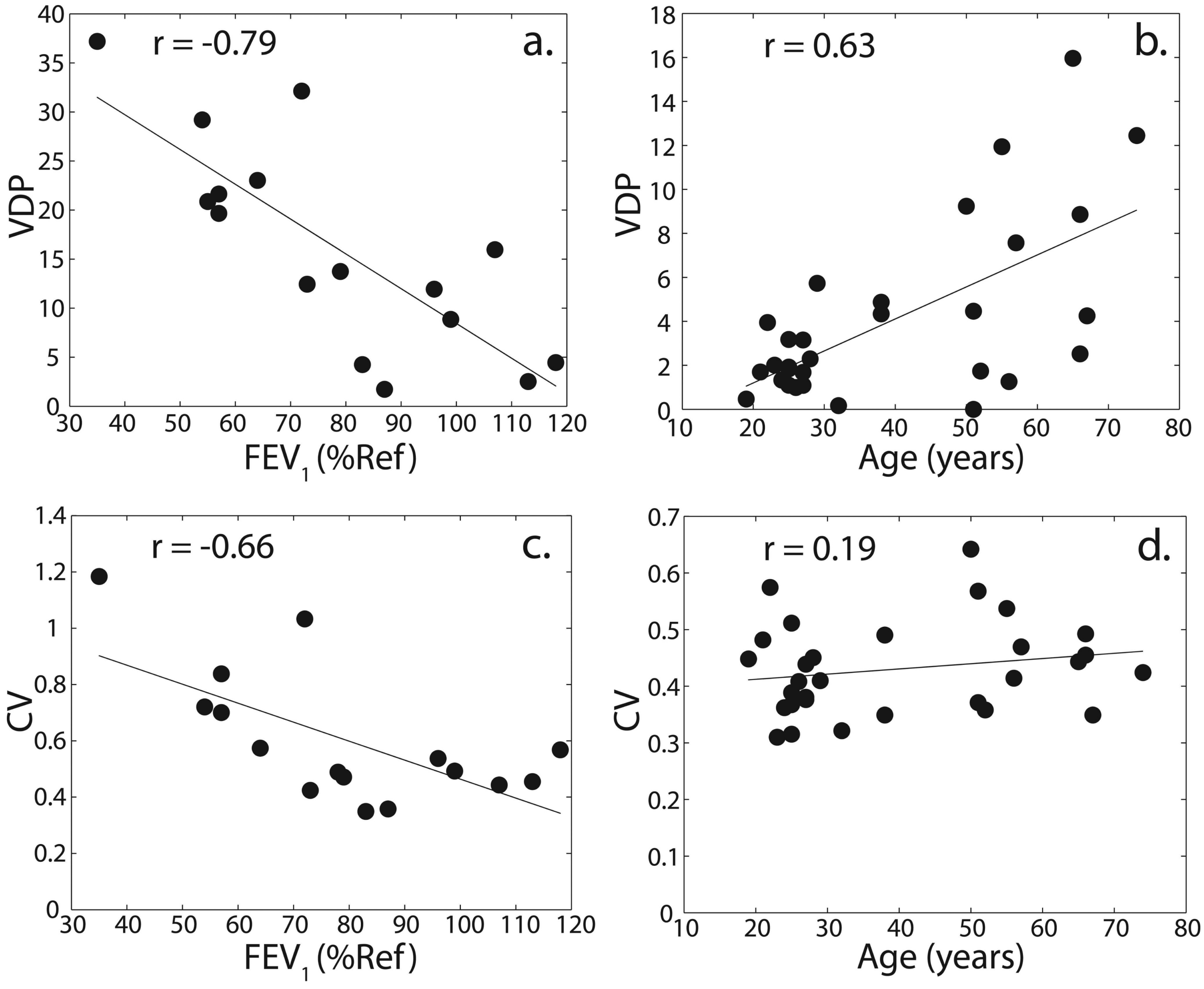

Figure 8.

Correlation of VDP and CV with FEV$_1$ (a, c) and with subject age (b, d).

Table 1

Mean values (±SD) of VDS%, VDP, and CV.

	VDS%	**VDP**	**CV**
		Mean Values	
HV	3.03 ± 5.17%	2.72 ± 2.39%	0.42 ± 0.08
AMC	13.0 ± 10.3%	7.77 ± 5.27%	0.45 ± 0.08
COPD	47.4 ± 11.6%	24.7 ± 7.6%	0.75 ± 0.26
	p-values for comparisons between subject groups		
HV, AMC	$p < 0.0001$	$p < 0.0001$	$p = 0.34$ [a]
HV, COPD	$p = 0.0009$	$p = 0.0014$	$p = 0.0003$
AMC, COPD	$p = 0.0099$	$p = 0.0070$	$p = 0.0024$

[a] not statistically significant

Table 2

Correlations (r) of VDS%, VDP and CV with PFTs and age.

	VDS%	VDP	CV
FEV_1	-0.80 (p = 0.0002)	-0.79 (p = 0.0003)	-0.66 (p = 0.0059)
FEV_1/FVC	-0.75 (p = 0.0008)	-0.71 (p = 0.0022)	-0.71 (p = 0.0019)
Dl_{co}	-0.83 (p < 0.0001)	-0.85 (p < 0.0001)	-0.73 (p = 0.0014)
Dl_{co}/Va	-0.70 (p = 0.0032)	-0.68 (p = 0.0081)	-0.71 (p = 0.0025)
Age	0.61 (p = 0.0002)	0.63 (p =0.0002)	0.19 (p = 0.30) [a]

[a] not statistically significant